Scientific Reports

https://doi.org/10.1038/s41598-026-38895-9

Article in Press

Oxidative stress-mediated impairment of human trophoblast cell proliferation by zinc pyrithione exposure

Received: 19 October 2025

Accepted: 31 January 2026

Published online: 05 February 2026

Cite this article as: Wang X., Luo B., Lu Z. *et al.* Oxidative stress-mediated impairment of human trophoblast cell proliferation by zinc pyrithione exposure. *Sci Rep* (2026). https://doi.org/10.1038/s41598-026-38895-9

Xiumei Wang, Bingbing Luo, Ziqin Lu, Xiangxue Cai, Junling Wang & Junbiao Mao

Title: Oxidative Stress-Mediated Impairment of Human Trophoblast Cell Proliferation by Zinc Pyrithione Exposure

Xiumei Wang [1,2,3,+], Bingbing Luo [2,3,+], Ziqin Lu [1,2,3], Xiangxue Cai [2,3], Junling Wang[2,3,*], Junbiao Mao [2,3,*]

1.Department of Reproductive Medicine, Huangshi Central Hospital Graduate Joint Training Base, School of Medicine, Wuhan University of Science and Technology, Wuhan, 430000, P. R. China.

2.Huangshi Key Laboratory of Assisted Reproduction and Reproductive Medicine, Huangshi Central Hospital, Huangshi, 435000, P. R. China.

3.Department of Reproductive Medicine, Huangshi Central Hospital, Affiliated Hospital of Hubei Polytechnic University, Huangshi, 435000, P. R. China.

*Correspondence:

Junbiao Mao, No. 141 Tianjin Road, Huangshigang District, Huangshi 435000, Hubei, China. Email: junbiaomao@163.com

Junling Wang, No. 141 Tianjin Road, Huangshigang District, Huangshi 435000, Hubei, China. Email: Wjl225969@163.com

+.These authors contributed equally to this work.

Abstract: Zinc pyrithione (ZPT), a broad-spectrum antimicrobial agent widely used in anti-dandruff shampoos and antifouling coatings, has an unclear toxic effect on embryonic trophoblast cells. To systematically evaluate the toxicological impact of ZPT on human trophoblast cell line JEG-3 and its underlying mechanisms, cells were treated with 90 nM ZPT for 72 hours. A series of assays, including Cell Counting Kit-8(CCK-8), flow cytometry, wound healing, and Transwell, were performed to assess cell proliferation, apoptosis, migration, and invasion. Intracellular reactive oxygen species (ROS) levels and DNA damage were assessed using the 2′,7′-dichlorodihydrofluorescein diacetate (DCFH-DA) probe and γ-H2AX immunofluorescence, respectively. Transcriptome sequencing and Gene Ontology(GO) enrichment analysis were also performed. The results indicated that ZPT significantly inhibited cell proliferation, migration, and invasion, induced late-stage apoptosis, and increased ROS levels and DNA damage. RNA sequencing (RNA-seq) identified 1020 differentially expressed genes, suggesting an upregulation in autophagy and mitochondrial apoptosis pathways, and a significant downregulation in glycolysis, NAD^+ regeneration, and hypoxia response pathways. Quantitative real-time polymerase chain reaction (qPCR) validation further confirmed the upregulation of key stress- and autophagy-related genes (NUPR1, SQSTM1) and the downregulation of genes involved in trophoblast function and mitochondrial quality control (BMP4, BNIP3, BNIP3L). These in vitro findings suggest that ZPT may impair trophoblast function through mechanisms involving oxidative stress, DNA damage, and perturbations in mitochondrial apoptosis/autophagy and energy metabolism.

Keywords: Zinc pyrithione; trophoblast cells; oxidative stress; apoptosis; transcriptome

1. Introduction

Zinc pyrithione (ZPT, molecular formula $C_{10}H_8N_2O_2S_2Zn$) is a 1:2 complex formed between zinc ions and pyrithione ligands, and exhibits broad-spectrum antifungal, antibacterial, and antialgal properties. Its low solubility and particulate-based nature underpin its widespread use in pharmaceuticals, personal care products (e.g., anti-dandruff shampoos), and industrial antifouling coatings[1]. However, with increasing consumption, ZPT continues to accumulate in aquatic environments, particularly in coastal waters and sediments affected by industrial wastewater discharges. Environmental concentrations of ZPT have been reported in the range of 0.04–0.32 μg/L[2], leading to its classification as an emerging contaminant. Although ZPT can undergo photodegradation, recent studies indicate this process is significantly slower or inhibited in shallow, high-clarity water environments, which may prolong its environmental persistence and potential impact[3]. Furthermore, the degradation of ZPT yields potentially toxic by-products, including pyrithione (PT)—which can accumulate in sediments at concentrations up to 420 μg/kg dry weight[4]—and zinc ions (Zn^{2+}); the release of Zn^{2+} contributes to heavy metal pollution[5]. Moreover, ZPT demonstrates a pronounced potential for bioaccumulation. For example, in the digestive gland of the Mediterranean mussel (Mytilus galloprovincialis), ZPT and PT have been measured at up to 0.1 and 0.01 μmol/g wet weight, respectively, highlighting a tangible ecological risk[6].

Numerous studies have indicated that even low concentrations of ZPT exhibit significant toxicity to aquatic organisms, with generally low median effective concentration (EC_{50}) or median lethal concentration (LC_{50}) values reported in fish, algae, and crustaceans[7]. Furthermore, embryonic developmental abnormalities and growth inhibition have been observed in various species, including zebrafish, mussels, and sea urchins, following ZPT exposure[8,9]. Sublethal concentrations of ZPT have also been shown to induce oxidative stress and DNA damage in marine polychaetes, leading to significant suppression of growth and survival[10]. Given its environmental prevalence, human exposure routes primarily include dermal contact and dietary intake[11,12]. Holmes et al. reported that repeated use of a ZPT-containing shampoo over four days resulted in deposition levels of up to 2602 μg on the scalp and hands[11]. Topical application for 48 hours increased zinc concentrations in the viable epidermis approximately 250-fold compared to controls, indicating significant zinc accumulation facilitated by ZPT. While dermal exposure is a confirmed pathway, dietary intake may represent a more significant route for systemic exposure. A study on crucian carp (a common farmed fish in China) found that ZPT accumulates in and is retained by tissues such as the liver and kidneys[12]. Consequently, the toxicological effects of ZPT and its potential implications for human health have become a major focus of risk assessment. In vitro studies suggest that ZPT may alter neurodevelopment-related gene expression, inhibit neurite outgrowth, and trigger oxidative stress and mitochondrial dysfunction, contributing to cytotoxicity and neurotoxicity[13]. Moreover, ZPT has been shown to exacerbate intracellular zinc accumulation and oxidative stress in HepG2 cells, resulting in apoptosis[14]. As a common ingredient in personal care products, an in-depth investigation into the toxic effects of ZPT on human cells is essential for a comprehensive assessment of its potential health risks.

Although the reproductive toxicity of ZPT toward aquatic organisms and mammalian gametes has been increasingly recognized, its toxicity at the embryonic level—particularly its impact on trophoblast cells, which are critical for early pregnancy—remains poorly understood. Trophoblast cells play an essential role in embryonic development, contributing to implantation, fetal growth, and pregnancy maintenance. Dysfunction of these cells is closely associated with adverse pregnancy outcomes, including unexplained embryonic arrest and miscarriage[15]. Existing studies have indicated that ZPT can induce embryonic developmental toxicity in organisms such as zebrafish, manifesting as spinal malformation, pericardial edema, and hatching delay. The underlying mechanisms involve oxidative stress, endoplasmic reticulum stress, and autophagy[16]. Furthermore, ZPT has been shown to increase the risk of aneuploid embryos—the most common genetic cause of early miscarriage—via zinc accumulation, spindle defects mediated by microtubule-organizing center (MTOC)-associated proteins, and alterations in epigenetic modifications[17]. While direct epidemiological evidence linking ZPT to human miscarriage remains to be established through large-scale studies, the multiplicity of its toxic mechanisms suggests that ZPT may disrupt trophoblast function and elevate the risk of pregnancy failure.

Therefore, this study utilized the human embryonic trophoblast cell line JEG-3 as a model to systematically investigate the effects of ZPT on the physiological functions of trophoblast cells. We assessed ZPT-induced cytotoxicity by measuring changes in cell proliferation, apoptosis, migration, and invasion. To elucidate the role of oxidative stress, we measured ROS levels, DNA damage, and indicators related to energy metabolism. Furthermore, transcriptomic sequencing was used to explore potential regulatory networks underlying ZPT-induced trophoblast dysfunction. Quantitative real-time polymerase chain reaction (qPCR) was used to verify the expression levels of key differential genes identified by

transcriptomic analysis. This in vitro study aims to provide experimental evidence for understanding the mechanisms underlying ZPT's developmental toxicity.

2. Materials and Methods

2.1 Cell culture, reagents, and instruments

Zinc pyrithione (ZPT, MedChemExpress, HY-B0572) was prepared as a 40 mM stock solution in dimethyl sulfoxide (DMSO) and stored at -20°C. Before each experiment, the stock solution was serially diluted with fresh cell culture medium to achieve the desired working concentrations. The final concentration of DMSO in all treatment groups, including the vehicle control, was maintained at 0.1% (v/v) to eliminate potential solvent toxicity effects. JEG-3 cells were seeded into culture plates and incubated overnight to ensure complete attachment prior to experimental treatments. JEG-3 cells were cultured in high-glucose Dulbecco's Modified Eagle Medium (DMEM) supplemented with 10% fetal bovine serum (FBS) (Vistech, SE200-ES) and 1% penicillin–streptomycin (100 U/mL), and maintained at 37 °C in a humidified atmosphere of 5% CO_2. The culture medium was renewed every two days. Subculturing was performed when cells reached 80–90% confluence.

2.2 Cell Viability Assay

JEG-3 cells in the logarithmic growth phase were washed with phosphate-buffered saline (PBS), detached using 0.25% trypsin, and seeded into 96-well plates at a density of 1.2×10^3 cells per well. After overnight incubation at 37 °C under 5% CO_2 to allow cell attachment, the culture medium was replaced with fresh medium containing ZPT at concentrations of 45, 90, and 180 nM. The ZPT treatment concentrations (90 nM and 180 nM) were selected based on preliminary dose–response experiments and represent the lowest levels that consistently induced statistically significant cytotoxicity and functional impairment in JEG-3 cells under the applied experimental conditions. Each concentration was tested in triplicate,

while control cells received an equal volume of medium alone. Following treatment for 24, 48, 72, 96, and 120 hours, 100 µL of CCK-8 solution (Biosharp, NO: BS350B) was added to each well, and the plates were incubated for 2 hours in the dark. The optical density (OD) was measured at 450 nm using a microplate reader. Cell Viability (%) = $[(OD_{treat} - OD_{vehicle}) / (OD_{control} - OD_{vehicle})] \times 100\%$, where $OD_{vehicle}$ represents wells containing CCK-8 reagent and culture medium without cells.. The experiment was independently repeated three times

2.3 Cell Apoptosis assay

JEG-3 cells in the logarithmic growth phase were trypsinized, resuspended, and seeded into culture dishes at a density of 2.0×10^5 cells per dish. After overnight incubation at 37 °C in a 5% CO_2 atmosphere, the cells were treated with 90 nM ZPT for 72 hours, while control groups received an equal volume of fresh medium. Following treatment, both the culture supernatant and trypsin-detached cells were collected, washed twice with PBS, and resuspended in 500 µL of 1× binding buffer. Subsequently, 5 µL of propidium iodide (PI) and 10 µL of Annexin V-FITC (Lianke Biotechnology, AP101) were added, and the cells were incubated in the dark for 15 minutes. Apoptosis was analyzed using flow cytometry. The experiment was independently repeated three times.

2.4 Cell Cycle Analysis

JEG-3 cells in the logarithmic growth phase were washed with PBS, detached by trypsinization, and seeded into culture dishes at a density of 2.0×10 5cells per dish. After overnight incubation at 37 °C in a 5% CO_2 atmosphere to facilitate attachment, cells were treated with 90 nM ZPT for 72 hours, while control groups received an equivalent volume of medium. Following treatment, cells were washed twice with PBS, harvested by trypsinization, and centrifuged at 1000 rpm for 3 minutes. The pellet was resuspended in ice-cold PBS, followed by the addition of 1 mL DNA staining solution and 10

μL permeabilization solution (Lianke Biotechnology, CCS012). After vortex mixing, the samples were incubated at room temperature for 30 minutes in the dark. The samples were analyzed using a flow cytometer at the minimum acquisition rate. The experiment was independently repeated three times.

2.5 Wound Healing Assay

JEG-3 cells in the logarithmic growth phase were washed with PBS, detached by trypsinization, and seeded into 6-well plates at a density of 2.0×10^5 cells per well. Cells were cultured at 37 °C under 5% CO_2 until approximately 80% confluence was reached. A uniform wound was created in the cell monolayer using a sterile 200 μL pipette tip. After gentle washing with PBS to remove detached cells, the control group was incubated with serum-free medium, while the experimental group received serum-free medium containing 90 nM ZPT. Images of the wound area were captured at 0, 24, 48, and 72 hours using an inverted microscope. Cell migration was quantified by measuring the wound width using ImageJ software. The width at 0 h (W_0) and at each subsequent time point (W_t) was recorded. The relative migration distance (%) was calculated as $[(W_0 – W_t) / W_0] \times 100\%$, representing the percentage of wound closure relative to the initial width. The experiment was independently repeated three times.

2.6 Transwell Invasion Assay

Transwell chambers were pre-coated with 60 μL of diluted Matrigel (1:8 dilution) under pre-cooled conditions and incubated at 37 °C for 30 minutes to promote solidification. The coated membranes were then hydrated with serum-free medium for 30 minutes. JEG-3 cells in the logarithmic growth phase were trypsinized and resuspended in either serum-free medium (control group) or serum-free medium containing 90 nM ZPT (experimental group). Cells were seeded into the upper chamber at a density of 7×10^3 cells per well in 200 μL of the respective medium. The lower chamber was filled with complete

medium containing 10% FBS as a chemoattractant. After 72 hours of incubation, invaded cells on the lower surface of the membrane were fixed with 4% paraformaldehyde for 20 minutes and stained with 0.1% crystal violet for 30 minutes. Non-invading cells on the upper surface were then gently removed with a cotton swab. The number of invaded cells was counted in five randomly selected fields per membrane under an inverted microscope. The experiment was independently repeated three times.

2.7 Intracellular ROS Level Detection

JEG-3 cells in the logarithmic growth phase were washed with PBS, detached by trypsinization, and seeded into 6-well plates at a density of 3×10^4 cells per well. After overnight incubation at 37 °C in a 5% CO_2 atmosphere, cells were treated with 90 nM ZPT for 72 hours. A positive control group was exposed to the ROS inducer Rosup (10 μM) for 20 minutes. Following treatment, cells were incubated with 10 μM DCFH-DA (Beyotime, S0033S) probe at 37 °C for 20 minutes in the dark. After washing twice with serum-free medium, the cells were harvested by trypsinization, resuspended in PBS, and immediately analyzed using a flow cytometer with excitation at 488 nm and emission at 525 nm. The experiment was independently repeated three times.

2.8 Immunofluorescence Detection of γ-H2AX

Sterile coverslips were placed in 24-well plates and coated with 0.1% gelatin solution for 1 hour. JEG-3 cells in the logarithmic growth phase were seeded at a density of 7.5 × 10^4 cells per well and cultured at 37°C under 5% CO_2 until 80% confluence was achieved. The experimental group was treated with 90 nM ZPT for 72 hours, while the control group received an equal volume of culture medium. After treatment, cells were washed twice with PBS and fixed with 4% paraformaldehyde at room temperature for 15 minutes. Following permeabilization with 0.3% Triton X-100 and blocking with 5% bovine serum albumin (BSA), the cells were incubated with an anti-

γ-H2AX primary antibody (Beyotime, C2035S) overnight at 4 °C, followed by incubation with a 488-conjugated secondary antibody for 1 hour at room temperature in the dark. Nuclei were counterstained with DAPI for 5 minutes. Coverslips were mounted with antifade mounting medium and imaged under a fluorescence microscope. The fluorescence intensity of γ-H2AX foci in the nuclei was quantified using ImageJ software. The experiment was independently repeated three times.

2.9 RNA-seq and data analysis

JEG-3 cells were cultured in high-glucose DMEM supplemented with 10% FBS and 1% penicillin–streptomycin at 37 °C under 5% CO_2. A control group and a 90 nM ZPT-treated group were established, each with three biological replicates. After cell attachment, the treatment was administered for 72 hours. Prior to cell collection, the culture medium was aspirated and discarded. Cells were washed twice with PBS, detached by trypsinization, and pelleted by centrifugation at 1000 rpm for 3 minutes. The cell pellet was resuspended in 100 µL of PBS, transferred to cryovials, flash-frozen in liquid nitrogen, and stored at −80 °C. Subsequently, total RNA was extracted from the cell pellets for RNA-seq analysis using the RNAprep Pure Cell Kit (centrifugal column type; Cat. No. DP430) according to the manufacturer's instructions. RNA concentration was quantified with the Qubit RNA Assay Kit (Life Technologies) on a Qubit 2.0 Fluorometer, and integrity was assessed using the RNA Nano 6000 Assay Kit (Agilent 5400 system; Agilent Technologies, DNF-471), with all samples showing RIN > 8.0. Sequencing libraries were then constructed with the Fast RNA-seq Lib Prep Kit V2 (ABclonal; Cat. No. RK20306): mRNA was enriched from 1 µg total RNA using poly-T magnetic beads, fragmented, and converted into cDNA, followed by end repair, A-tailing, adapter ligation, and size selection with the AMPure XP system (Beckman Coulter). The libraries were amplified on an ABI2720 PCR system (Applied Biosystems), purified, and their

quality was verified using the Agilent 5400 system. Libraries were pooled and sequenced on a DNBSEQ-T7 platform (MGI) in 150 bp paired-end mode. Raw data were subjected to quality control and filtering, followed by alignment to the human reference genome (GRCh38, GENCODE release 38) using STAR (version 2.7.10a). Gene expression quantification was performed with featureCounts (v2.0.3), and transcript assembly and quantification were conducted using StringTie (v2.2.1). Differential expression analysis was carried out with DESeq2 (v1.40.2), with significantly differentially expressed genes (DEGs) defined as those with $P<0.05$ and $|\log2(FC)|>0$. Gene Ontology (GO) enrichment analysis of significant DEGs was performed using the R package clusterProfiler (v4.10.0), with an adjusted $P<0.05$ set as the threshold for significant enrichment.

2.10 qPCR and data analysis

JEG-3 cells were cultured in high-glucose DMEM supplemented with 10% fetal bovine FBS and 1% penicillin-streptomycin at 37 °C under 5% CO_2, with a control group and a group treated with 90 nM ZPT established for comparison. After treatment, cells were washed twice with PBS and lysed using TRIzol reagent. The lysate was homogenized by gentle agitation and repeated pipetting, incubated at room temperature for 5 min, followed by the addition of chloroform. The mixture was vortexed vigorously for 15 s, incubated for 2–3 min at room temperature, and centrifuged for 15 min at 4 °C. The aqueous layer was carefully collected, mixed with isopropanol to precipitate RNA, and after 10 min at room temperature, centrifuged for 10 min at 4 °C. The resulting RNA pellet was washed twice with ice-cold 75% ethanol, air-dried in a laminar flow hood for 8–10 min, and dissolved in RNase-free water. RNA concentration and purity were measured with a NanoDrop 2000 spectrophotometer (Thermo Fisher Scientific). Reverse transcription was performed using the HiScript III RT SuperMix for qPCR (+gDNA wiper) (Vazyme, Cat# R323-01) according to the manufacturer's

instructions, whereby total RNA was combined with 4× gDNA wiper Mix and RNase-free water, incubated at 42 °C for 2 min, supplemented with 5× HiScript III qRT SuperMix II, and then reacted at 50 °C for 15 min before termination at 85 °C for 5 s. Quantitative PCR was subsequently carried out on a real-time PCR system using ChamQ Universal SYBR qPCR Master Mix (Vazyme, Cat# Q711-02), with each reaction containing 2× SYBR Green Master Mix, cDNA, forward and reverse primers（Hecegene, Table1）, and nuclease-free water, all run in triplicate in 96-well plates. The thermal cycling protocol comprised an initial denaturation at 95 °C for 5 min, 39 cycles of 95 °C for 15 s and 60 °C for 30 s, and a final melt-curve stage from 65 °C to 95 °C to verify amplification specificity. Relative gene expression was calculated using the $2-\Delta\Delta Ct$ method, with GAPDH as the internal reference gene. The experiment was independently repeated three times.

2.11 Statistical Analysis

Statistical analysis was performed using GraphPad Prism software (version 8.0). All data are presented as the mean ± standard deviation (SD). Comparisons between two groups were conducted using paired or unpaired Student's t-test, as appropriate. Comparisons among multiple groups were analyzed by one-way ANOVA followed by LSD post hoc test. A p-value of <0.05 was considered statistically significant.

3. Results

3.1 ZPT Inhibits the Proliferation of JEG-3 Cells

The CCK-8 assay indicated that ZPT treatment inhibited JEG-3 cell viability in a dose- and time-dependent manner (Figure 1). At 45 nM, ZPT did not significantly affect cell viability at any time point compared to the control ($P > 0.05$). In the 90 nM group, a significant reduction in viability was observed after 24 hours ($P < 0.01$), and this inhibition became more pronounced with prolonged exposure up to 120 hours ($P < 0.01$ at all later time points). Treatment with 180

nM ZPT resulted in significant inhibition as early as 24 hours ($P < 0.01$), which further intensified at 48 and 72 hours ($P < 0.01$), and remained significant through 96 and 120 hours ($P < 0.01$). Collectively, these results demonstrate that ZPT suppresses trophoblast proliferation in a manner dependent on both concentration and duration of exposure.

3.2 ZPT Induces Apoptosis Without Affecting Cell Cycle Progression in JEG-3 Cells

To investigate whether ZPT induces apoptosis, we examined the apoptotic rate of JEG-3 cells after treatment with 90 nM ZPT for 72 hours. Flow cytometric analysis demonstrated a marked increase in the late apoptotic cell population following ZPT treatment compared to the control, in which the rate of late apoptosis remained low (Figure 2A). Quantitative results revealed a significant increase in the proportion of late apoptotic cells in the treated group ($P < 0.05$; Figure 2B). Furthermore, to examine whether ZPT affects cell cycle distribution, we analyzed changes in the cell cycle following the same treatment protocol (Figure 2C). The results showed no significant alterations in the proportions of cells in the G_0/G_1, S, or G_2/M phases between the treated and control groups ($P > 0.05$; Figure 2D). These findings indicate that 90 nM ZPT effectively induces late apoptosis in JEG-3 cells with statistical significance, but does not elicit detectable disruption of cell cycle progression in JEG-3 cells.

3.3 ZPT Inhibits Migration and Invasion of JEG-3 Cells

To investigate the effects of ZPT on trophoblast motility, we assessed the migratory and invasive capacities of JEG-3 cells after treatment with 90 nM ZPT. The wound healing assay revealed a marked impairment of cell migration in the treated group at 48 hours compared to the control (Figure 3A). Quantitative analysis demonstrated that the wound closure rate was significantly reduced in the ZPT-treated group at 24, 48, and 72 hours ($P < 0.05$, Figure

3C). The Transwell invasion assay showed a noticeable reduction in the number of cells penetrating the Matrigel matrix in the treated group (Figure 3B). Consistent with the invasion assay results, the number of invading cells was significantly decreased following ZPT exposure compared to the control ($P < 0.05$, Figure 3D). These findings indicate that 90 nM ZPT significantly inhibits both the migratory and invasive capabilities of JEG-3 cells.

3.4 ZPT Induces Oxidative Stress and DNA Damage in JEG-3 Cells

To investigate the effects of ZPT on DNA damage and intracellular ROS levels in JEG-3 cells, DNA double-strand breaks were evaluated by immunofluorescence staining of γ-H2AX (Figure 4A). The results showed that treatment with 90 nM ZPT for 72 hours significantly enhanced γ-H2AX fluorescence intensity compared to the control group ($P < 0.05$; Figure 4B), indicating substantial DNA damage in JEG-3 cells. ROS production was quantified using flow cytometry (Figure 4C), which revealed a significant increase in ROS-associated fluorescence intensity following the same treatment ($P < 0.05$; Figure 4D), demonstrating marked induction of oxidative stress. These findings collectively indicate that 90 nM ZPT exposure induces both DNA damage and oxidative stress in JEG-3 cells.

3.5 Transcriptomic Profiling Reveals ZPT-Induced Dysregulation in JEG-3 Cells

Transcriptomic analysis was performed on JEG-3 cells treated with 90 nM ZPT for 72 hours. A sample correlation heatmap showed high intra-group correlations (0.97–0.99) but reduced inter-group similarity (Figure 5A). Principal component analysis (PCA) illustrated a clear separation between control and ZPT-treated samples along PC1 (84.7% variance), with treated cells forming a distinct cluster (Figure 5B). The volcano plot identified 975 differentially expressed genes (DEGs), comprising 488 upregulated

and 487 downregulated genes, against a background of 14,830 stable genes (Figure 5C).

Gene Ontology (GO) enrichment analysis revealed distinct patterns for up- and down-regulated DEGs. Upregulated DEGs were significantly enriched in biological processes related to cellular responses to starvation, unfolded proteins, and nutrient levels (-log10(p-value) 8–10), as well as intrinsic apoptotic signaling, endoplasmic reticulum stress, and the regulation of autophagy and catabolic processes (Figure 5D). Conversely, downregulated DEGs showed significant enrichment in metabolic and adaptive pathways, including sterol biosynthesis, NAD metabolism and catabolism, canonical glycolysis, glucose catabolism to pyruvate, NADH regeneration, and responses to hypoxia and oxygen levels (-log10(p-value) 5–10) (Figure 5E).

In summary, the transcriptomic analysis results indicate that ZPT exposure induces a dual molecular effect in JEG-3 cells: on one hand, it coordinately activates stress and cell death-related pathways, while on the other hand, it broadly suppresses core metabolic and adaptive functions.

3.6 qRT-PCR Validation Confirms ZPT-Induced Transcriptional Changes in Key Genes

To validate the RNA-seq results, quantitative real-time PCR (qRT-PCR) was performed on five representative differentially expressed genes in JEG-3 cells. As shown in Figure 6, ZPT treatment significantly up-regulated the mRNA expression of NUPR1 and SQSTM1 compared with the control group (both **$p < 0.01$). In contrast, the expression of BMP4, BNIP3, and BNIP3L was significantly down-regulated (**$p < 0.01$ and *$p < 0.05$, respectively). These qRT-PCR results are f consistent with the transcriptomic data and confirm the differential expression patterns of genes associated with cellular stress response, autophagy, and trophoblast function following ZPT exposure.

4.Discussion

During embryonic development, trophoblast cells are essential for establishing the embryo-maternal interface and placental formation. Their invasive and differentiated nature also renders them particularly sensitive to environmental toxicants, including heavy metals, organic pollutants, and pharmaceutical compounds. Dysfunction of these cells is closely linked to adverse pregnancy outcomes, such as implantation failure, pregnancy loss, and fetal developmental abnormalities. Zinc pyrithione (ZPT), a widely used antimicrobial agent in consumer products and agricultural applications , has not been systematically evaluated for its potential toxicity toward embryonic trophoblast cells. Therefore, this study employed the human trophoblast cell line JEG-3 to evaluate the cytotoxic effects of ZPT and explore its underlying mechanisms. Through multi-dimensional experiments including assessments of cell proliferation, apoptosis, migration, invasion, reactive oxygen species (ROS) levels, DNA damage, and transcriptomic sequencing, we indicated that ZPT induced oxidative stress and DNA damage, significantly inhibited cell viability, promoted apoptosis, and impaired migratory and invasive capacities. RNA sequencing further suggested that these toxic effects were closely associated with dysregulated autophagy, activation of the intrinsic apoptotic signaling pathway, and suppression of key energy metabolism processes such as glycolysis and NAD^+ regeneration. These transcriptional alterations were further supported by qRT-PCR validation, which confirmed the upregulation of stress- and autophagy-related genes (e.g., NUPR1, SQSTM1) and the downregulation of genes involved in trophoblast development and mitochondrial quality control (e.g., BMP4, BNIP3, BNIP3L)

The present study demonstrated via CCK-8 assay that ZPT significantly inhibited JEG-3 cells proliferation after 24 hours of treatment at concentrations exceeding 90 nM. Exposure to 180 nM ZPT reduced cell viability to negligible levels, indicating that ZPT

suppresses JEG-3 cells viability in a concentration-dependent manner. Flow cytometric analysis further confirmed that ZPT treatment significantly increased the rate of apoptosis. Cellular apoptosis is primarily triggered through the extrinsic (death receptor-mediated) and intrinsic (mitochondria-mediated) signaling pathways, which converge on the activation of executioner caspases-3/7[18]. GO enrichment analysis revealed significant enrichment of genes associated with the intrinsic apoptotic pathway. This pathway is characterized by loss of mitochondrial membrane potential, ROS burst, and cytochrome c release, leading to sequential activation of caspase-9 and caspase-3. Notably, BNIP3 and BNIP3L act as important regulators of mitochondrial apoptosis[19]. In trophoblast cells, these proteins promote cell death by counteracting BCL2 family members, triggering mitochondrial outer membrane permeabilization (MOMP), and facilitating cytochrome c release and caspase activation[20]. However, qRT-PCR analysis in this study revealed reduced expression of both BNIP3 and BNIP3L—a finding that seems inconsistent with the observed activation of mitochondrial apoptosis. This apparent paradox may indicate an adaptive cellular reprogramming in response to persistent ZPT exposure. Downregulation of BNIP3/BNIP3L could serve to prevent excessive mitophagy and the resulting energy depletion, while apoptosis may proceed via alternative pathways such as ROS accumulation and the DNA damage-p53 axis. Together, these observations underscore the multifaceted and context-dependent mechanisms through which ZPT induces apoptosis in trophoblast cells. Multiple studies have reported ZPT-induced activation of the mitochondrial apoptotic pathway in HepG2 cells, lymphocytes, and zebrafish embryos [14,16,21], which is consistent with our findings. The aberrant accumulation of ROS is a key initiating event in the aforementioned processes. This study demonstrated that ZPT significantly increased intracellular ROS levels in JEG-3 cells. Nuclear protein 1 (NUPR1) functions as a key stress-response marker, and its transcription is rapidly activated under oxidative stress[22]. qRT-PCR analysis confirmed that NUPR1 expression was significantly upregulated in ZPT-treated JEG-3 cells. This upregulation aligns with the elevated intracellular ROS levels detected in our study, together providing consistent evidence that

ZPT induces a state of oxidative stress in trophoblast cells. Excessive ROS can directly cause DNA damage, which was confirmed in this study by the significant increase in γ-H2AX foci formation following ZPT treatment. Although no significant cell cycle arrest was observed in the present study, this may be related to the specific cellular response to damage signals. The canonical DNA damage response pathway—wherein p53 activation triggers mitochondrial outer membrane permeabilization, cytochrome c release, and ultimately caspase cascade activation[23]—provides a plausible mechanistic explanation for these observations. Taken together, the observed DNA damage (indicated by increased γ-H2AX foci), the transcriptional signature associated with intrinsic apoptosis, and the upregulation of the stress marker NUPR1 suggest that under the present experimental conditions, ZPT-induced cell death appears to be driven predominantly by ROS-mediated DNA damage and subsequent activation of the mitochondrial apoptotic pathway, rather than by sustained cell cycle arrest.

In addition to inducing apoptosis, ZPT significantly impaired the functional properties of JEG-3 cells. Wound healing and Transwell invasion assays showed that ZPT treatment markedly reduced both migration distance and the number of invading cells, indicating that ZPT not only decreases cell number but also directly disrupts migratory and invasive capabilities. Trophoblast cells rely on the epithelial–mesenchymal transition (EMT) process to acquire migratory and invasive phenotypes, which are essential for successful embryo implantation and placental development. Bone morphogenetic protein 4 (BMP4), a member of the transforming growth factor-β (TGF-β) superfamily, plays a key regulatory role in cell proliferation and differentiation during embryonic development[24] and its expression level is known to influence the migration and invasion capacities of trophoblast cells[25].qRT-PCR analysis in this study revealed that BMP4 expression was significantly downregulated in ZPT-treated JEG-3 cells. The downregulation of BMP4 signaling may serve as one of the hubs linking ZPT exposure to the downstream transcriptomic alterations

and functional phenotypes. Mechanistically, GO analysis revealed that down-regulated genes were significantly enriched in pathways such as hypoxia response, glycolysis, and NAD^+ metabolism, suggesting that ZPT may suppress cell migration by inhibiting HIF-1α stability, reducing the expression of EMT-related transcription factors (e.g., Snail, Twist), and impairing energy support from glycolysis[26,27]. The downregulation of BMP4, which can itself be regulated by hypoxia and participate in EMT and metabolic processes, might form part of this broader dysregulated network[28]. Dysregulated NAD^+ metabolism may also indirectly interfere with EMT through modulation of Sirtuin deacetylase activity [29,30]. These pathways constitute an interconnected regulatory network where hypoxia signaling acts as an upstream initiator, EMT serves as the phenotypic executor, and glycolytic and NAD^+ metabolic reprogramming provide the metabolic basis. How precisely ZPT perturbs this finely tuned network, and the causal relationship between metabolic alterations and cellular behavior, requires further investigation. We speculate that ZPT impairs the migratory and invasive capacities of JEG-3 cells by destabilizing HIF-1α signaling, inducing metabolic dysfunction (e.g., suppressing glycolysis and depleting NAD^+), and downregulating developmental signals such as BMP4. Further studies using Western blotting, immunofluorescence, metabolomic profiling, and NAD^+ measurements could help clarify ZPT's effects on EMT markers and test the causal relationship between metabolic reprogramming and the observed functional impairments.

The specific molecular mechanisms by which ZPT induces apoptosis in human embryonic trophoblast cells during early embryonic development remain incompletely elucidated. Oxidative stress, which directly regulates trophoblast function by modulating metabolic, autophagic, and apoptotic pathways[31], represents a critical mechanism in the pathogenesis of pregnancy-related disorders. Our data suggest that ZPT exposure may initiate cellular

stress, notably by increasing oxidative burden. We observed that ZPT treatment significantly elevated intracellular ROS levels in JEG-3 cells. This finding is consistent with prior reports in zebrafish sperm, where ZPT altered the activity of antioxidant enzymes such as GPx, CAT, and SOD, disturbing hydrogen peroxide metabolism and lipid peroxidation[23]. While elevated ROS may contribute to cytotoxicity, its role as a central trigger for downstream events in trophoblast cells requires further validation. ZPT treatment was associated with changes in autophagy-related pathways. Research indicates that ROS accumulation in the endoplasmic reticulum (ER) exacerbates oxidative stress, which in turn aggravates ER stress by impairing protein folding, forming a self-amplifying loop that promotes autophagy activation[32,33]. The marked upregulation of autophagy-related pathways observed in this study aligns with changes in the expression of autophagy marker genes atg5, beclin1 (atg6), and atg16l2 reported in zebrafish embryos[16,34].Additionally, we detected upregulation of SQSTM1, an autophagy adaptor involved in ubiquitinated cargo delivery. This may indicate altered autophagic activity, although functional assays are needed to confirm autophagic flux changes[35]. The interplay among oxidative stress, ER stress, and autophagy may influence mitochondrial apoptosis under ZPT exposure. Excessive ROS can potentially damage mitochondrial DNA and function[31]. Moreover, ER stress sensors such as PERK and IRE1α, along with pro-apoptotic factors like Chop[36], could contribute to mitochondrial apoptotic signaling[36].which is consistent with the apoptotic transcriptional profile observed in this study. ZPT has previously been shown to promote apoptosis in HepG2 cells by inducing mitochondrial dysfunction, reducing the Bcl-2/Bax ratio, and activating caspase-3/9. These observations are in line with studies in HepG2 cells where ZPT was linked to mitochondrial dysfunction, altered Bcl-2/Bax ratio, and caspase-3/9 activation[14]. In our transcriptomic data, apoptotic pathways were enriched. Notably, expression of the mitophagy

regulators BNIP3 and BNIP3L was downregulated. BNIP3 helps maintain ROS homeostasis and promotes mitochondrial turnover[37]. Previous studies suggest that BNIP3 inhibition can impair mitophagy, leading to ROS accumulation and apoptosis[38]. Our flow cytometry data showed increased ROS levels in ZPT-treated cells, which may be related to BNIP3 downregulation. However, whether BNIP3-mediated mitophagy dysregulation directly links oxidative stress to apoptosis in this model remains to be experimentally verified.

In addition to apoptosis-related changes, ZPT exposure was associated with reduced trophoblast migration and invasion in vitro. We found downregulation of BMP4, a gene involved in trophoblast development and motility. Altered BNIP3 expression might also affect mitochondrial energetics and thereby impair invasive capacity. Since trophoblast invasion is essential for placental establishment, these in vitro observations may have physiological relevance, though their in vivo significance is unclear. In summary, this study indicates that ZPT can induce oxidative stress, perturb autophagy and mitophagy-related gene expression, and activate apoptotic pathways in a trophoblast cell model. These effects may collectively contribute to reduced cell viability and impaired invasive behavior in vitro. However, the precise mechanistic cascade and its pathophysiological relevance necessitate further investigation using integrated functional approaches and more physiologically relevant models.

In summary, this in vitro study suggests that ZPT can trigger oxidative stress in human trophoblast cells, which may in turn disrupt autophagic balance, activate ER stress and the mitochondrial apoptotic pathway, and cause DNA damage. Together, these stress and damage responses form a cascade of functional disturbances that not only promote trophoblast apoptosis but also markedly impair their migration and invasion—key processes in placental development. The observed changes at the transcriptional level are

further supported by qPCR validation of relevant marker genes. This study establishes a mechanistic framework for understanding ZPT-induced trophoblast dysfunction, identifies candidate biomarkers of its effects, and provides a foundation for future work to assess whether ZPT exposure may interfere with early placental development or elevate pregnancy-related risks under more physiologically relevant conditions.

This study is primarily based on in vitro experiments using the JEG-3 cells and has several important limitations. The cellular model may not fully replicate the biological complexity of trophoblasts in vivo, and the proposed link between oxidative stress, autophagy, and apoptosis remains correlative, as causal relationships have not been functionally validated. The physiological or environmental relevance of the ZPT concentrations used in this experiment requires further evaluation. Most critically, all findings are confined to an in vitro context and lack validation through animal models or clinical samples; therefore, they cannot be directly extrapolated to the complex physiological or pathological processes of human pregnancy. To advance the understanding of ZPT reproductive toxicity, future work should include validation across more biologically relevant models—such as primary cells, 3D co-cultures, and animal studies—as well as mechanistic experiments using genetic or pharmacological approaches to confirm the roles of key molecular targets. Epidemiological studies could also help clarify whether real-world exposure levels are associated with adverse pregnancy outcomes. Together, these steps would strengthen the scientific foundation for assessing the safety risks of ZPT.

Author Contributions

JM and JW conceived and designed the research. XW and BL performed the experiment and analyzed the sequencing data. ZL, JM and XC performed the experiment. XW and JM wrote the original manuscript.

Funding

This work was supported by funding from the following sources: The Huangshi Health Commission General Research Project (WJ2024023); Hubei Provincial Natural Science Foundation (Joint Fund Project) (2023AFD019); Hubei Provincial Health Commission Fund (WJ2019H183); Huangshi Central Hospital Foundation Project (ZX2023M07).

Conflict of interest statement

The authors declare that they have no known competing financial interests or personal relationships that could have appeared to influence the work reported in this paper.

Data availability

All sequencing data related to this study have been deposited at Gene Expression Omnibus (GSA for Human, https://ngdc.cncb.ac.cn/gsa/) under the accession number HRA013363

References

1 Mangion, S. E., Holmes, A. M. & Roberts, M. S. Targeted Delivery of Zinc Pyrithione to Skin Epithelia. *Int J Mol Sci* **22**, doi:10.3390/ijms22189730 (2021).

2 Bones, J., Thomas, K. V. & Paull, B. Improved method for the determination of zinc pyrithione in environmental water samples incorporating on-line extraction and preconcentration coupled with liquid chromatography atmospheric pressure chemical ionisation mass spectrometry. *J Chromatogr A* **1132**, 157-164, doi:10.1016/j.chroma.2006.07.068 (2006).

3 Maraldo, K. & Dahllof, I. Indirect estimation of degradation time for zinc pyrithione and copper pyrithione in seawater. *Mar Pollut Bull* **48**, 894-901, doi:10.1016/j.marpolbul.2003.11.013 (2004).

4 Harino, H. *et al.* Concentrations of booster biocides in sediment and clams from Vietnam. *Journal of the Marine Biological Association of the United Kingdom* **86**, 1163-1170, doi:10.1017/s0025315406014147 (2006).

5 Marcheselli, M., Rustichelli, C. & Mauri, M. Novel antifouling agent zinc pyrithione: determination, acute toxicity, and bioaccumulation in marine mussels (Mytilus galloprovincialis). *Environ Toxicol Chem* **29**, 2583-2592, doi:10.1002/etc.316 (2010).

6 Marcheselli, M., Azzoni, P. & Mauri, M. Novel antifouling agent-zinc pyrithione:

stress induction and genotoxicity to the marine mussel Mytilus galloprovincialis. *Aquat Toxicol* **102**, 39-47, doi:10.1016/j.aquatox.2010.12.015 (2011).

7 Onduka, T. *et al.* Toxicity of metal pyrithione photodegradation products to marine organisms with indirect evidence for their presence in seawater. *Arch Environ Contam Toxicol* **58**, 991-997, doi:10.1007/s00244-009-9430-8 (2010).

8 Zhao, Y. *et al.* Acute toxic responses of embryo-larval zebrafish to zinc pyrithione (ZPT) reveal embryological and developmental toxicity. *Chemosphere* **205**, 62-70, doi:10.1016/j.chemosphere.2018.04.010 (2018).

9 Bellas, J., Granmo, Å. & Beiras, R. Embryotoxicity of the antifouling biocide zinc pyrithione to sea urchin (Paracentrotus lividus) and mussel (Mytilus edulis). *Marine Pollution Bulletin* **50**, 1382-1385 (2005).

10 Haque, M. N., Nam, S. E., Eom, H. J., Kim, S. K. & Rhee, J. S. Exposure to sublethal concentrations of zinc pyrithione inhibits growth and survival of marine polychaete through induction of oxidative stress and DNA damage. *Mar Pollut Bull* **156**, 111276, doi:10.1016/j.marpolbul.2020.111276 (2020).

11 Holmes, A. M., Kempson, I., Turnbull, T., Paterson, D. & Roberts, M. S. Imaging the penetration and distribution of zinc and zinc species after topical application of zinc pyrithione to human skin. *Toxicol Appl Pharmacol* **343**, 40-47, doi:10.1016/j.taap.2018.02.012 (2018).

12 Ren, T. *et al.* Toxicity and accumulation of zinc pyrithione in the liver and kidneys of Carassius auratus gibelio: association with P-glycoprotein expression. *Fish Physiol Biochem* **43**, 1-9, doi:10.1007/s10695-016-0262-y (2017).

13 Oh, H. N. & Kim, W. K. Copper pyrithione and zinc pyrithione induce cytotoxicity and neurotoxicity in neuronal/astrocytic co-cultured cells via oxidative stress. *Sci Rep* **13**, 23060, doi:10.1038/s41598-023-49740-8 (2023).

14 Mo, J., Lin, D., Wang, J., Li, P. & Liu, W. Apoptosis in HepG2 cells induced by zinc pyrithione via mitochondrial dysfunction pathway: Involvement of zinc accumulation and oxidative stress. *Ecotoxicol Environ Saf* **161**, 515-525, doi:10.1016/j.ecoenv.2018.06.026 (2018).

15 Sun, Q. & Zhang, X. L. Research on apoptotic signaling pathways of recurrent spontaneous abortion caused by dysfunction of trophoblast infiltration. *Eur Rev Med Pharmacol Sci* **21**, 12-19 (2017).

16 Zhao, Y. *et al.* Zinc pyrithione (ZPT) -induced embryonic toxicogenomic responses reveal involvement of oxidative damage, apoptosis, endoplasmic reticulum (ER) stress and autophagy. *Aquat Toxicol* **248**, 106195, doi:10.1016/j.aquatox.2022.106195 (2022).

17 Wang, Y. S. *et al.* Zinc pyrithione exposure compromises oocyte maturation through involving in spindle assembly and zinc accumulation. *Ecotoxicol Environ Saf* **234**, 113393, doi:10.1016/j.ecoenv.2022.113393 (2022).

18 Ma, H. *et al.* Identification and Functional Analysis of Apoptotic Protease

Activating Factor-1 (Apaf-1) from Spodoptera litura. *Insects* **12**, doi:10.3390/insects12010064 (2021).

19 Zhang, H. M., Cheung, P., Yanagawa, B., McManus, B. M. & Yang, D. C. BNips: a group of pro-apoptotic proteins in the Bcl-2 family. *Apoptosis* **8**, 229-236, doi:10.1023/a:1023616620970 (2003).

20 Wang, C. *et al.* Neutrophil extracellular traps aggravate placental injury in OAPS by facilitating activation of BNIP3 mediated mitophagy. *Free Radic Biol Med* **235**, 109-123, doi:10.1016/j.freeradbiomed.2025.04.038 (2025).

21 Mann, J. J. & Fraker, P. J. Zinc pyrithione induces apoptosis and increases expression of Bim. *Apoptosis* **10**, 369-379, doi:10.1007/s10495-005-0811-9 (2005).

22 Cano, C. E., Hamidi, T., Sandi, M. J. & Iovanna, J. L. Nupr1: the Swiss-knife of cancer. *J Cell Physiol* **226**, 1439-1443, doi:10.1002/jcp.22324 (2011).

23 Hu, J. *et al.* Toxic effects and potential mechanisms of zinc pyrithione (ZPT) exposure on sperm and testicular injury in zebrafish. *J Hazard Mater* **461**, 132575, doi:10.1016/j.jhazmat.2023.132575 (2024).

24 Hadas, R. *et al.* Temporal BMP4 effects on mouse embryonic and extraembryonic development. *Nature* **634**, 652-661, doi:10.1038/s41586-024-07937-5 (2024).

25 Tang, L. *et al.* Deletion of BMP4 impairs trophoblast function and decidual macrophage polarization via autophagy leading to recurrent spontaneous abortion. *Int Immunopharmacol* **147**, 114015, doi:10.1016/j.intimp.2025.114015 (2025).

26 Semenza, G. L. Hypoxia-inducible factors: mediators of cancer progression and targets for cancer therapy. *Trends Pharmacol Sci* **33**, 207-214, doi:10.1016/j.tips.2012.01.005 (2012).

27 Dong, C. *et al.* Loss of FBP1 by Snail-mediated repression provides metabolic advantages in basal-like breast cancer. *Cancer Cell* **23**, 316-331, doi:10.1016/j.ccr.2013.01.022 (2013).

28 Hong, J. W. *et al.* BMP4 Regulates EMT to be Involved in non-Syndromic Cleft lip With or Without Palate. *Cleft Palate Craniofac J* **60**, 1462-1473, doi:10.1177/10556656221105762 (2023).

29 Chiarugi, A., Dolle, C., Felici, R. & Ziegler, M. The NAD metabolome--a key determinant of cancer cell biology. *Nat Rev Cancer* **12**, 741-752, doi:10.1038/nrc3340 (2012).

30 Alberto, C., Christian, D., Roberta, F. & Mathias, Z. The NAD metabolome--a key determinant of cancer cell biology. *Nature reviews. Cancer* **12**, 741-752 (2012).

31 Guo, C., Sun, L., Chen, X. & Zhang, D. Oxidative stress, mitochondrial damage and neurodegenerative diseases. *Neural Regen Res* **8**, 2003-2014, doi:10.3969/j.issn.1673-5374.2013.21.009 (2013).

32 Plaisance, V. *et al.* Endoplasmic Reticulum Stress Links Oxidative Stress to Impaired Pancreatic Beta-Cell Function Caused by Human Oxidized LDL. *PLoS One* **11**, e0163046, doi:10.1371/journal.pone.0163046 (2016).

33 Gorlach, A., Bertram, K., Hudecova, S. & Krizanova, O. Calcium and ROS: A mutual interplay. *Redox Biol* **6**, 260-271, doi:10.1016/j.redox.2015.08.010 (2015).

34 Don Wai Luu, L., Kaakoush, N. O. & Castano-Rodriguez, N. The role of ATG16L2 in autophagy and disease. *Autophagy* **18**, 2537-2546, doi:10.1080/15548627.2022.2042783 (2022).

35 Lamark, T., Svenning, S. & Johansen, T. Regulation of selective autophagy: the p62/SQSTM1 paradigm. *Essays Biochem* **61**, 609-624, doi:10.1042/EBC20170035 (2017).

36 Verfaillie, T. *et al.* PERK is required at the ER-mitochondrial contact sites to convey apoptosis after ROS-based ER stress. *Cell Death Differ* **19**, 1880-1891, doi:10.1038/cdd.2012.74 (2012).

37 Burton, T. R. & Gibson, S. B. The role of Bcl-2 family member BNIP3 in cell death and disease: NIPping at the heels of cell death. *Cell Death Differ* **16**, 515-523, doi:10.1038/cdd.2008.185 (2009).

38 Zhou, X. *et al.* Impaired placental mitophagy and oxidative stress are associated with dysregulated BNIP3 in preeclampsia. *Sci Rep* **11**, 20469, doi:10.1038/s41598-021-99837-1 (2021).

Figure legends

Figure1. Effects of ZPT on Cell Viability

Cell viability was assessed using the CCK-8 assay after treatment with various concentrations (45, 90, and 180 nM) of ZPT for different durations (0–120 hours). The results are expressed as relative percentages compared to the control group (set as 100%). Statistical significance was analyzed relative to the control group. Data were obtained from at least three independent experiments and are presented as mean ± standard deviation (SD). *$p < 0.05$, **$p < 0.01$; ns: not significant.

Figure2. Effects of ZPT on Apoptosis and Cell Cycle

(A) Representative flow cytometry scatter plots of Annexin V-FITC/PI staining after 72-hour treatment with ZPT. The four quadrants represent viable cells (Annexin V^-/PI^-), early apoptotic cells (Annexin V^+/PI^-), late apoptotic cells (Annexin V^+/PI^+), and necrotic cells (Annexin V^-/PI^+). (B) Representative flow cytometry histograms of PI staining showing DNA content after 72-hour ZPT treatment. (C) Quantitative analysis of late apoptosis rate. Data are from three

independent experiments and expressed as mean ± SD. **p < 0.01. (D) Quantitative analysis of cell cycle distribution. The percentages of cells in each phase (G0/G1, S, G2/M) are summarized. Data are from three independent experiments and expressed as mean ± SD. ns: not significant.

Figure3. Effects of ZPT on Cell Migration and Invasion

(A) Representative images of the wound healing assay at different time points (40× magnification). (B) Representative images of Transwell cell invasion assay after crystal violet staining (100× magnification). (C) Quantitative analysis of wound healing rate. The migration rate of JEG-3 cells after ZPT treatment at various time points was compared with that of the control group. (D) Bar graph showing the number of invaded cells. Data are presented as mean ± SD from three independent experiments. (*p < 0.05, **p < 0.01).

Figure4. Effects of ZPT on Reactive Oxygen Species and DNA Damage

(A) Representative immunofluorescence images showing γ-H2A.X foci formation in JEG-3 cells from the control and 90 nM ZPT-treated groups. Cells were stained with an anti-γ-H2A.X antibody (green), and nuclei were counterstained with DAPI (blue). Scale bar: 30 μm. (B) Quantitative analysis of γ-H2A.X fluorescence intensity relative to the control group. Data were obtained from three independent experiments and are presented as mean ± SD, with each data point derived from five randomly selected fields per group (*p < 0.05). (C) Representative histograms of intracellular ROS production. A rightward shift indicates increased ROS levels. (D) Quantitative analysis of ROS fluorescence intensity relative to the control. Data are shown as mean ± SD from three independent experiments (**p < 0.01).

Figure5. Transcriptomic analysis of JEG-3 cells following treatment

(A) Heatmap of gene expression correlation among biological

replicates. (B) Principal component analysis (PCA) showing the distribution of transcriptomic profiles between the control and ZPT-treated groups. (C) Volcano plot of differentially expressed genes (threshold: $|\log_2(\text{fold change})| > 1$ and adjusted p-value < 0.05). Red dots denote significantly up-regulated genes, blue dots indicate significantly down-regulated genes, and gray dots represent non-significant genes. (D) GO biological process enrichment analysis of significantly up-regulated genes. (E) GO biological process enrichment analysis of significantly down-regulated genes. All experiments included three biological replicates. Differential expression analysis was performed using DESeq2, and genes with an adjusted p-value < 0.05 (Benjamini–Hochberg method) were considered statistically significant.

Figure 6. qPCR validation of selected differentially expressed genes in JEG-3 cells following treatment.

Quantitative analysis of relative mRNA expression levels (normalized to GAPDH) for NUPR1, SQSTM1, BMP4, BNIP3, and BNIP3L. Data are shown as mean ± SD from three independent experiments. Treatment with 90 nM ZPT resulted in significant up-regulation of NUPR1 and SQSTM1, and significant down-regulation of BMP4, BNIP3, and BNIP3L (**p < 0.01,*p < 0.05).

A

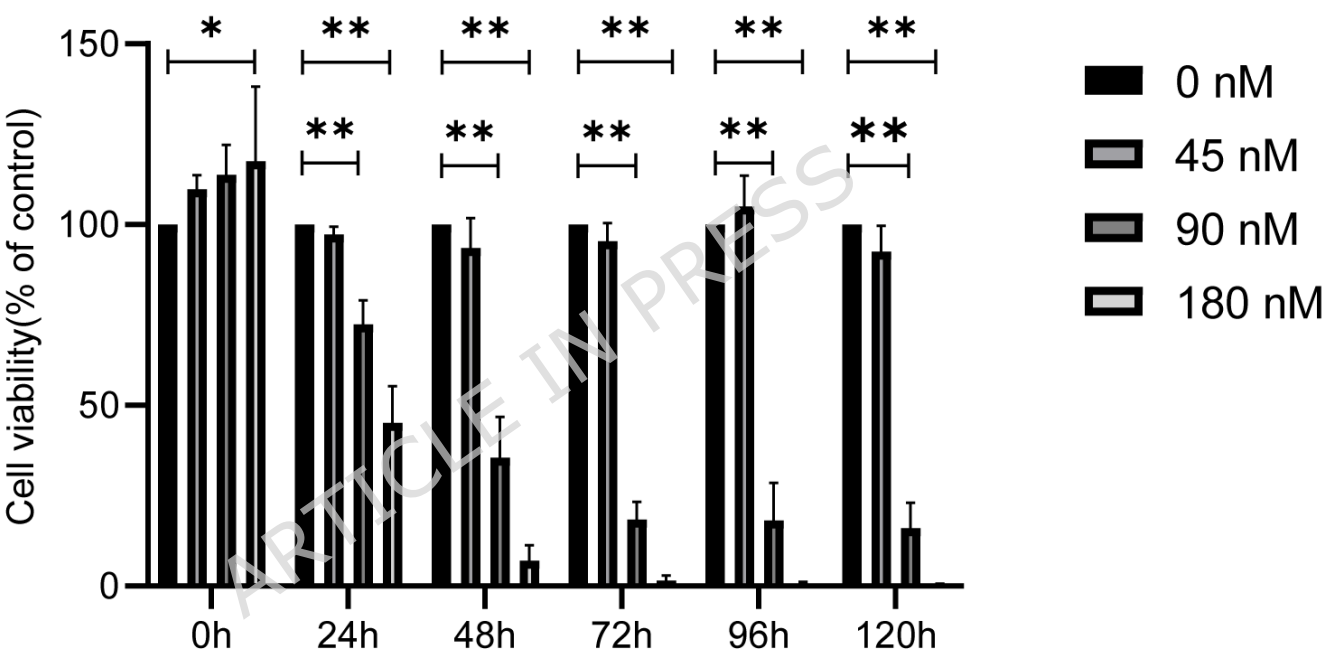

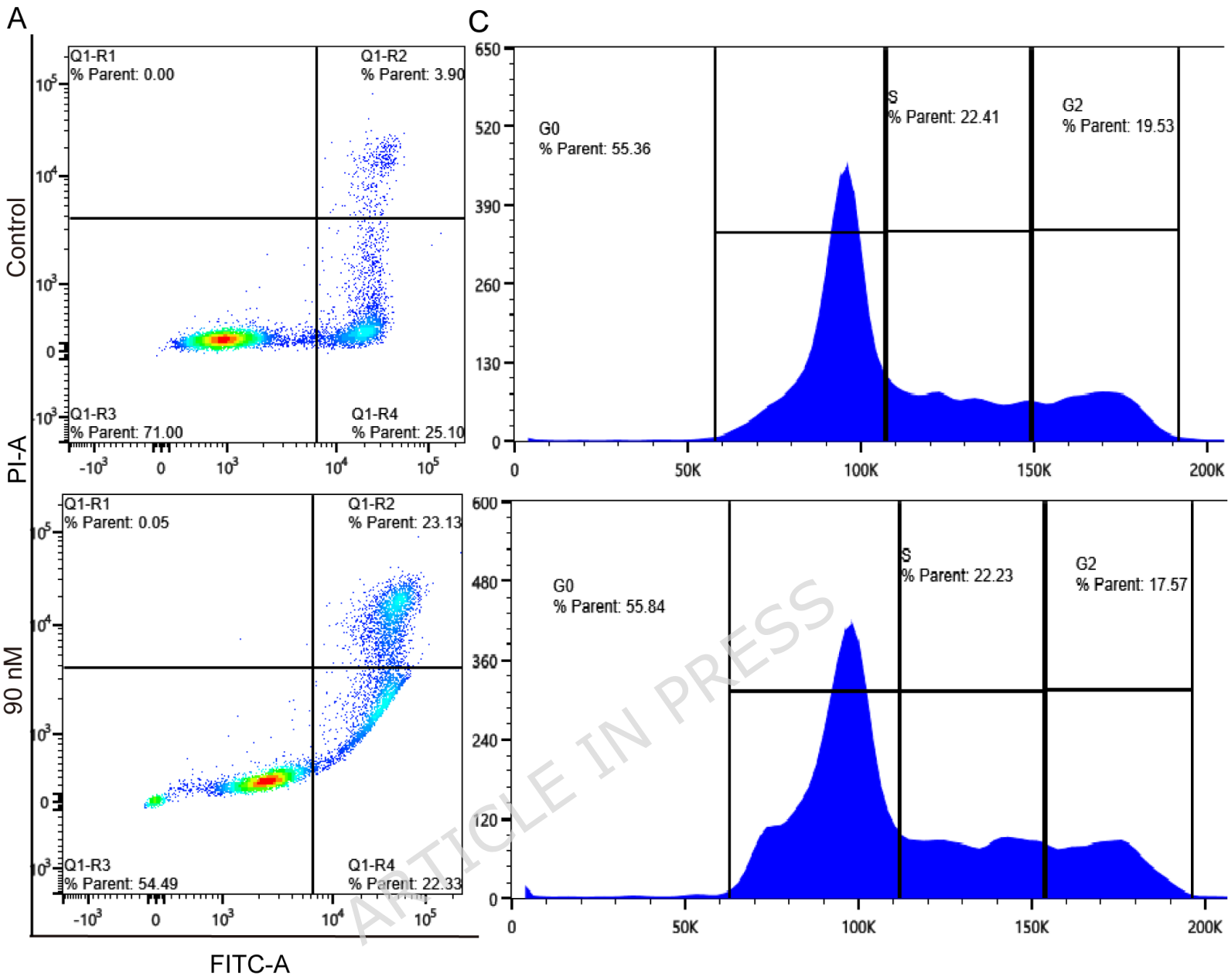

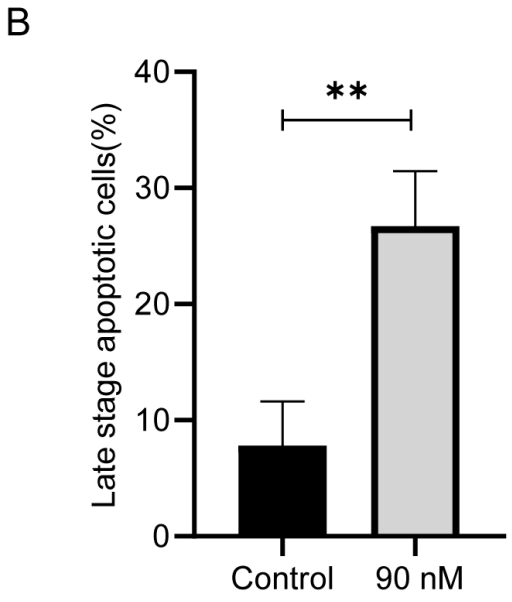

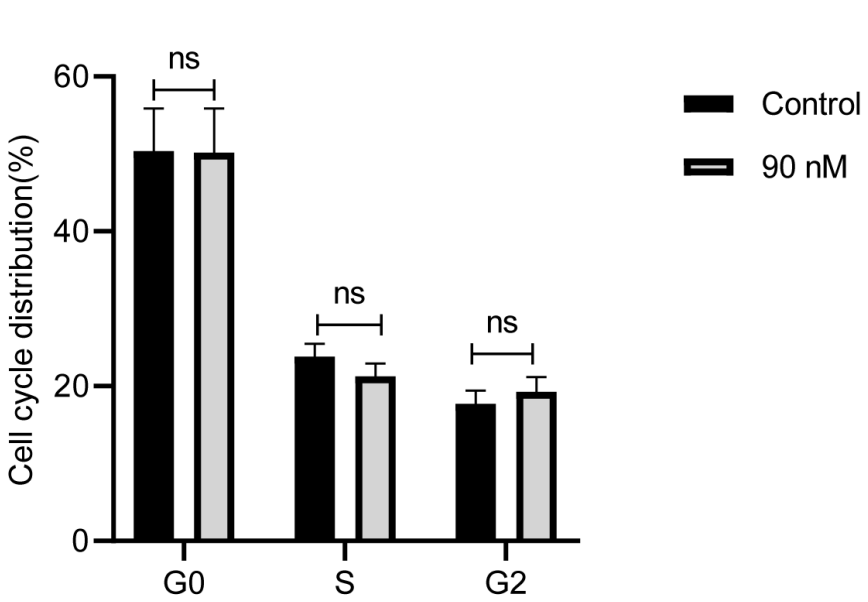

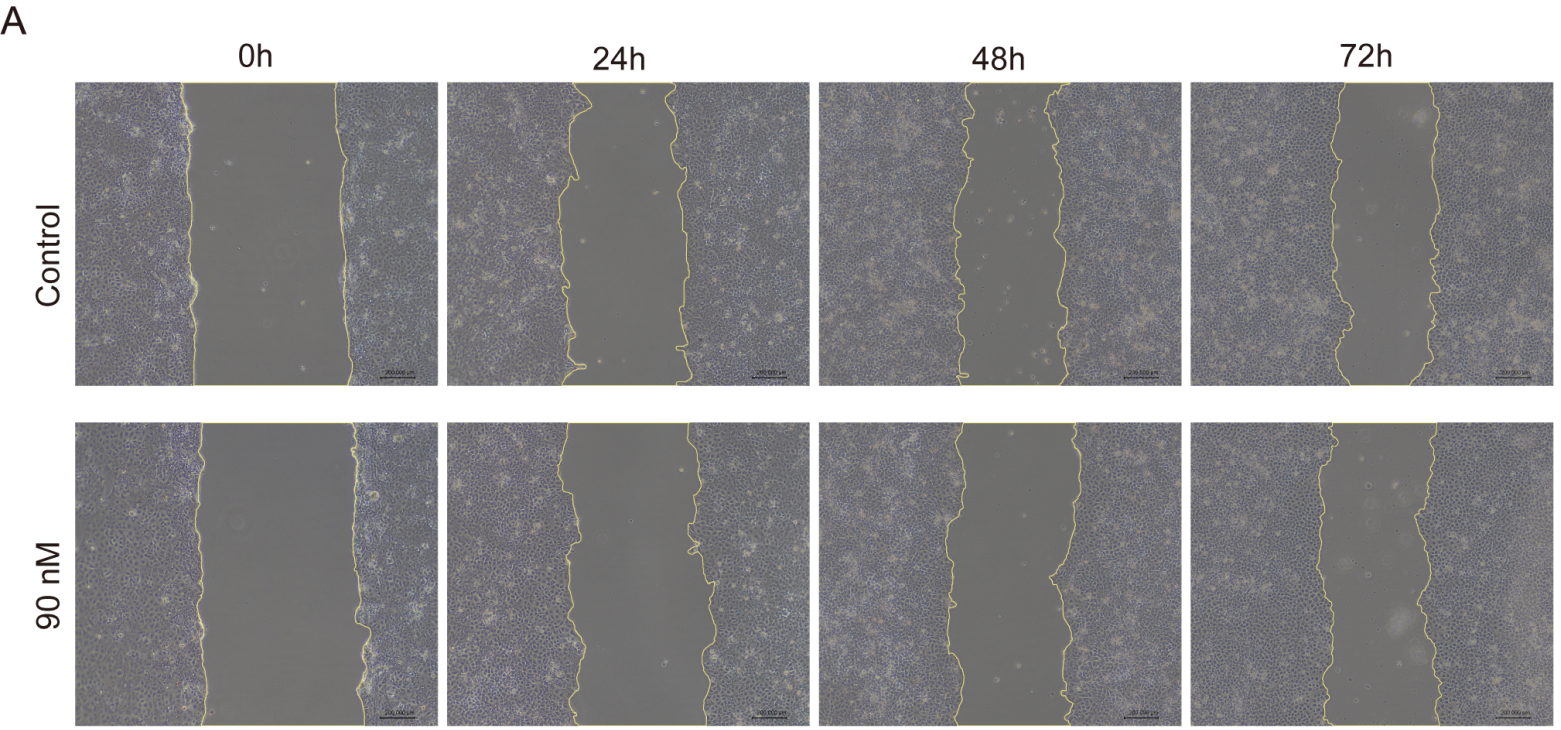

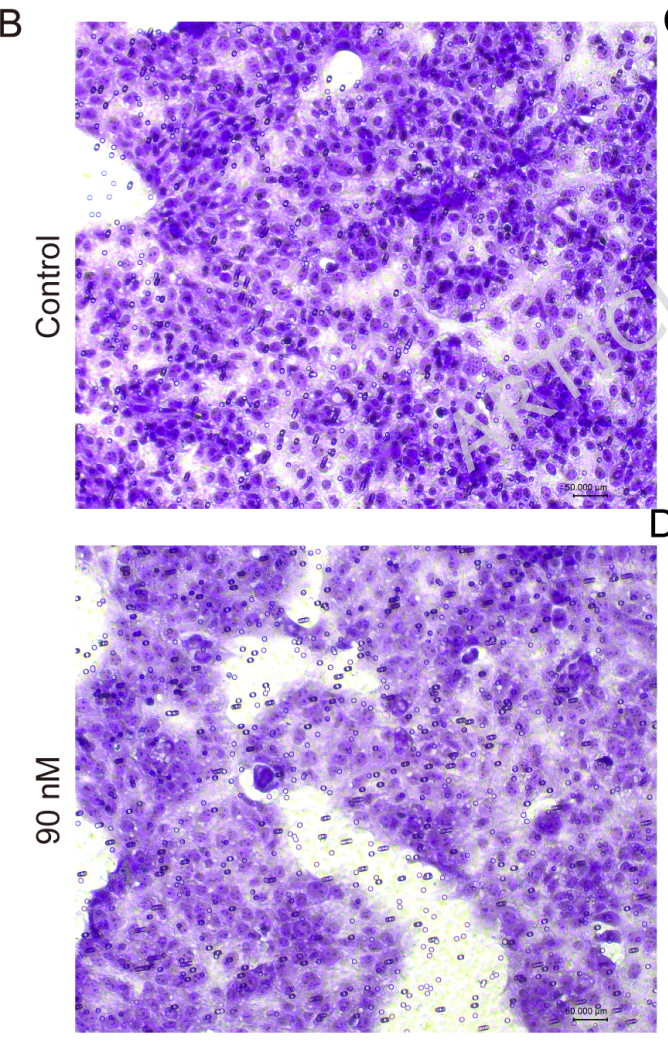

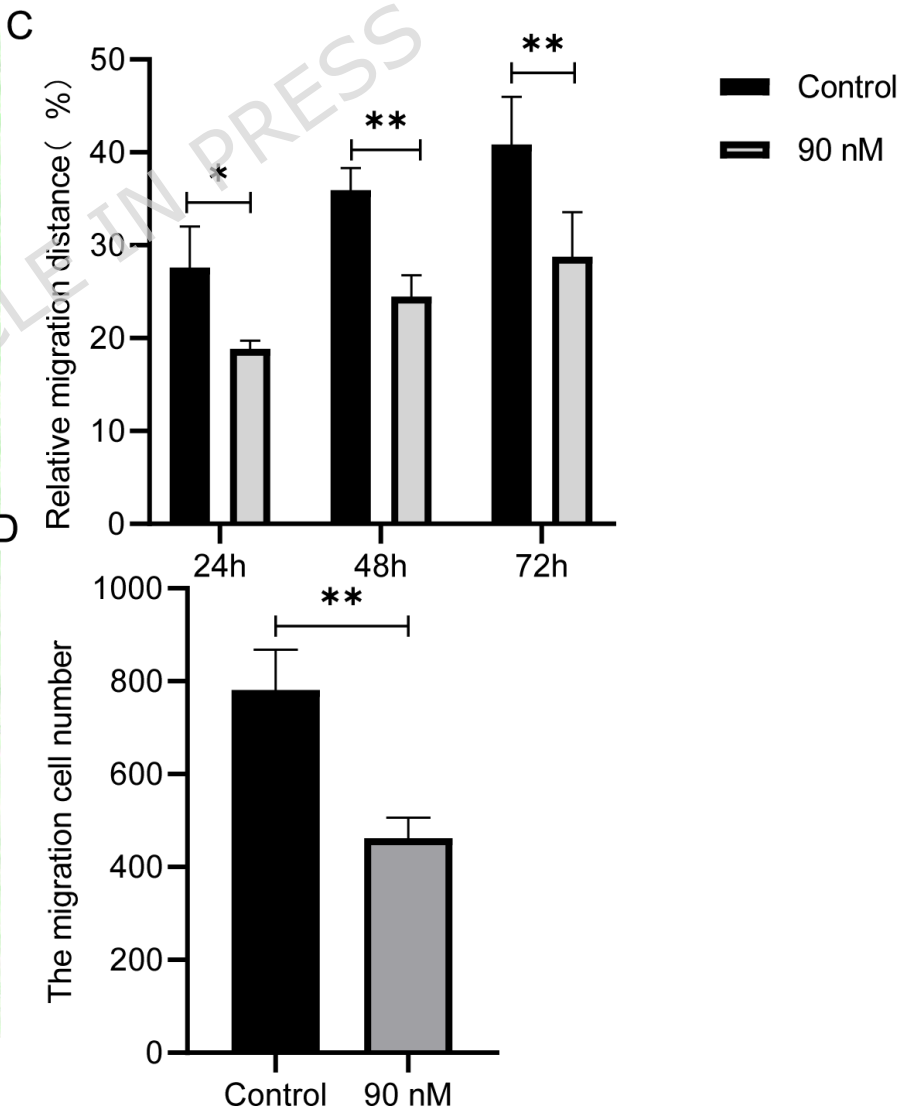

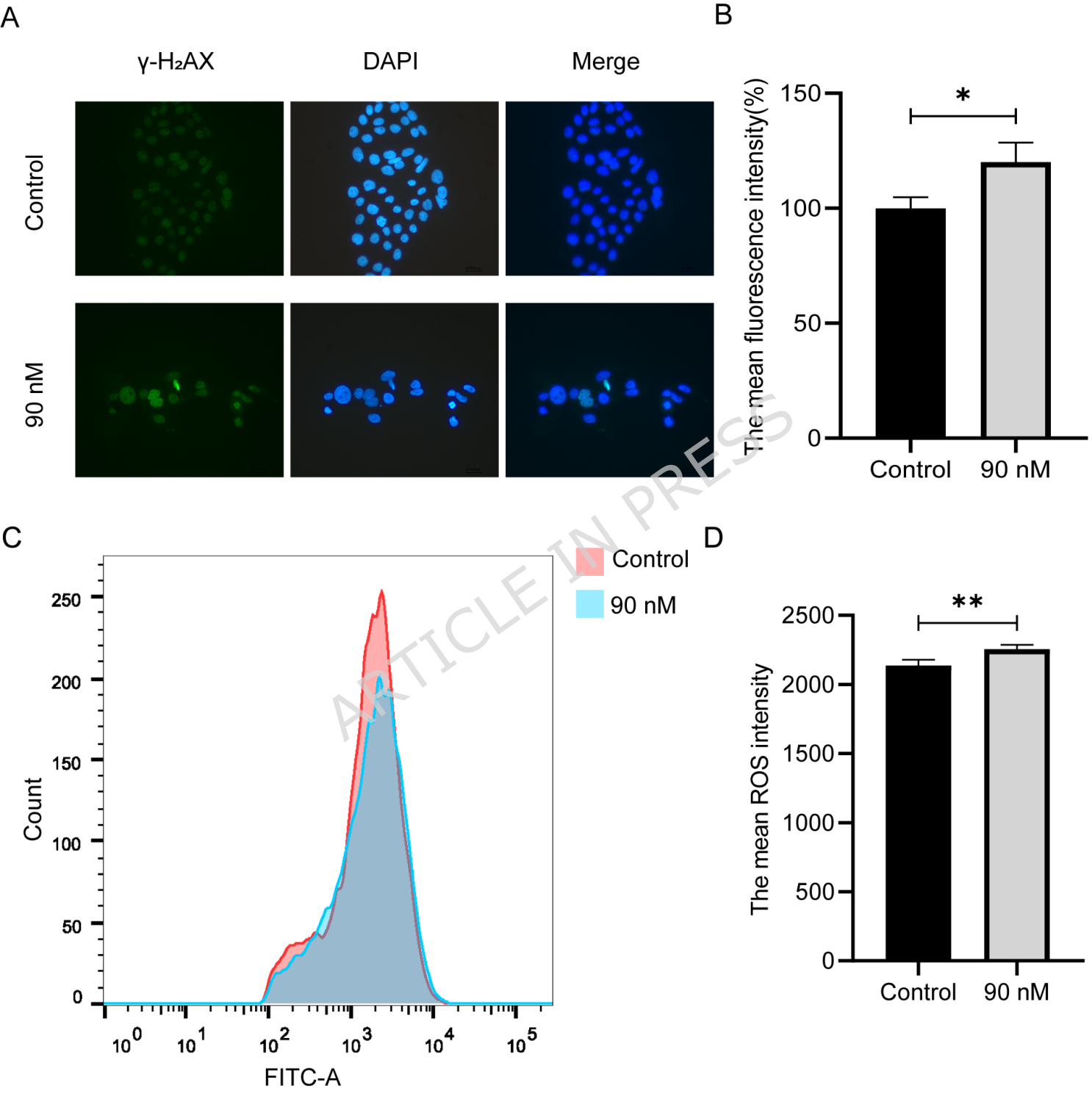

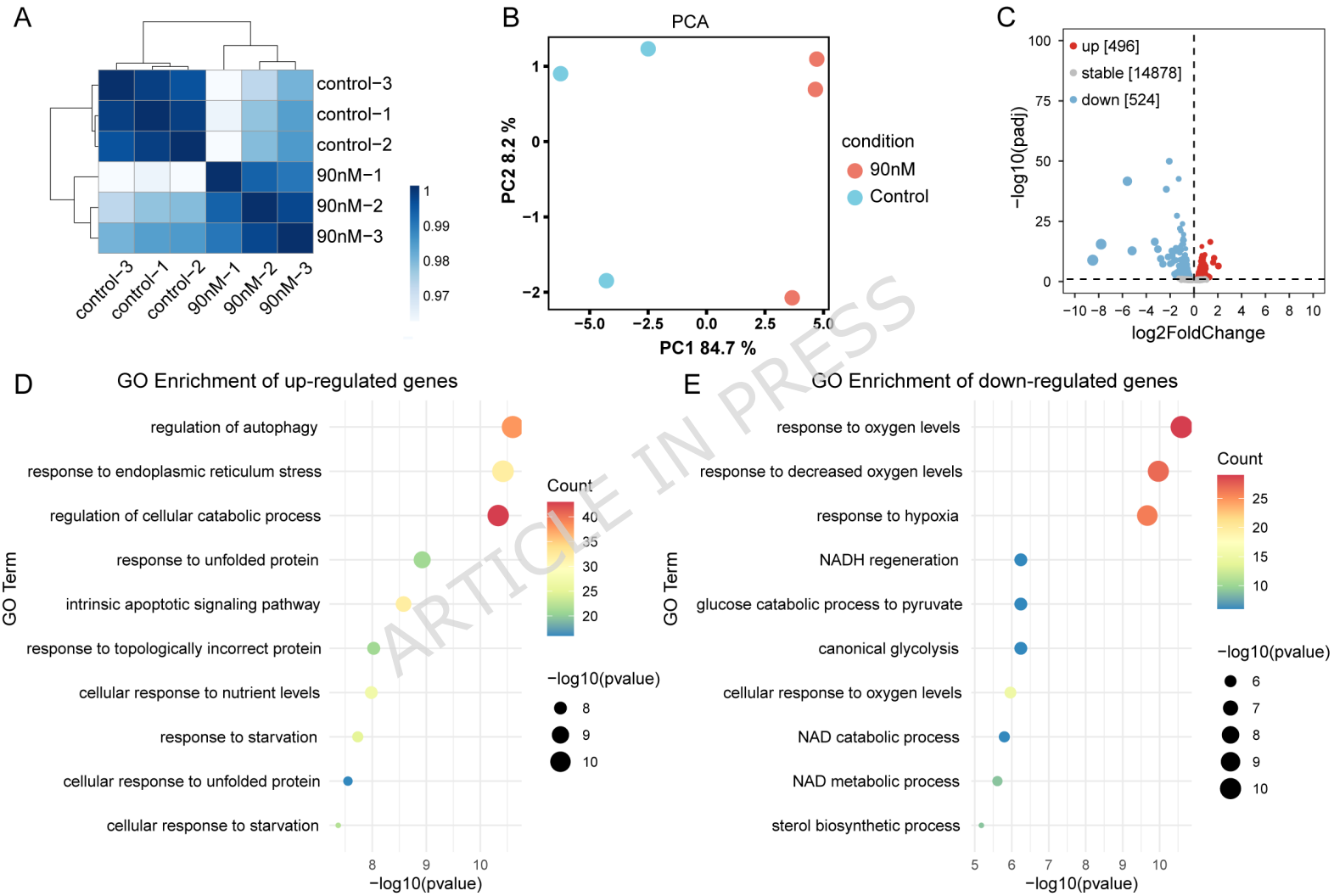

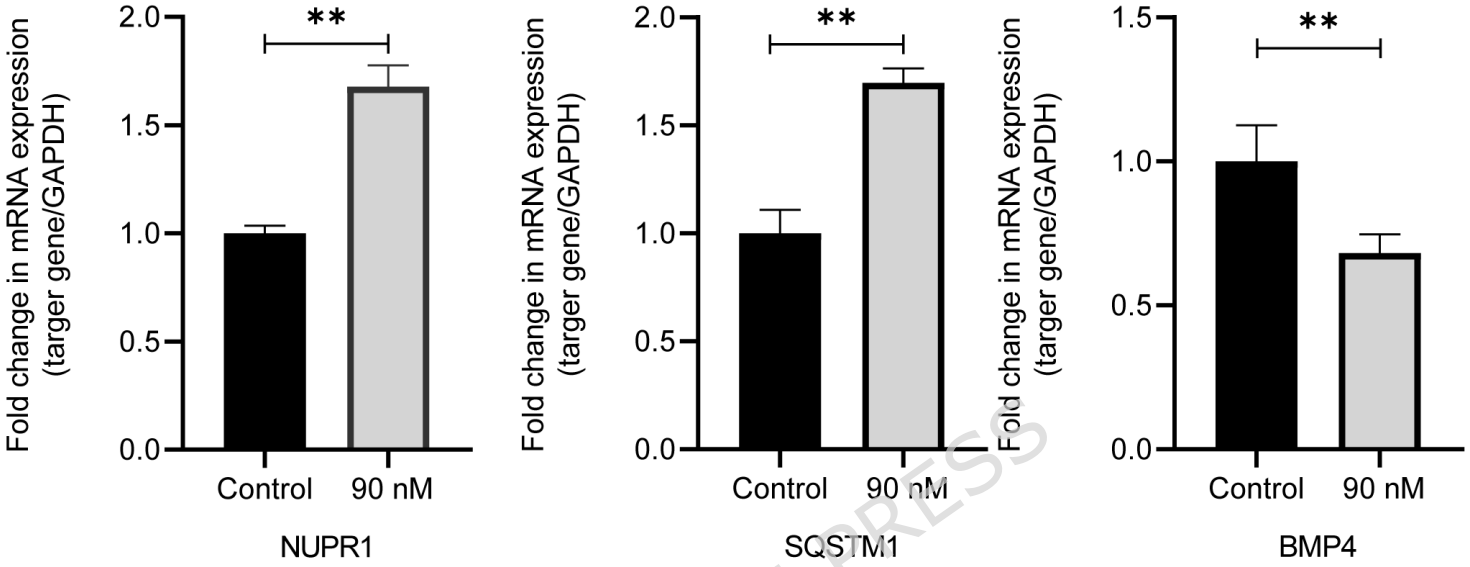

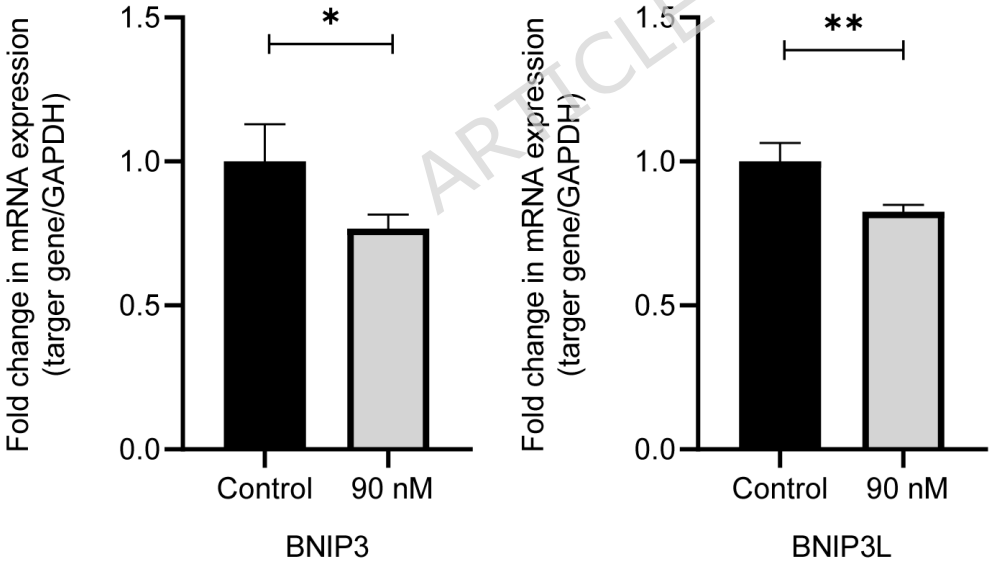

Table 1.

Primer sequences used for quantitative real-time PC

Gene	Forward primer (5′→3′)
GAPDH	AAAGGGTCATCATCTCTGCCCC
NUPR1	CCTCTATAGCCTGGCCCATTCC
SQSTM1	TGTGGAGCACGGAGGGAAAAGA
BMP4	GCCACTCGCTCTATGTGGAC
BNIP3	TCTCACTGTGACAGCCCACCTC
BNIP3L	CGGACTGGGTATCAGACTGGTC

GAPDH, glyceraldehyde-3-phosphate dehydrogenase; N
BMP4, bone morphogenetic protein 4; BNIP3/BNIP3L:

CR.

Reverse primer (5′→3′)
TGATGGCATGGACTGTGGTCAT
TGGTCACCAGTTTCCTCTCGTG
ACTCCATCTGTTCCTCAGGGCG
AGTAGAAGGCCTGGTAGCCT
GCCCCCTTTCTTCATGACGCTC
AGCCCCAAAGCCAAAACATGAG

NUPR1, nuclear protein 1; SQSTM1, sequestosome 1;
BCL2/adenovirus E1B 19 kDa protein-interacting protein 3 (and -like)

BMP4, bone morphogenetic protein 4; BNIP3/Bl

NIP3L: BCL2/adenovirus E1B 1